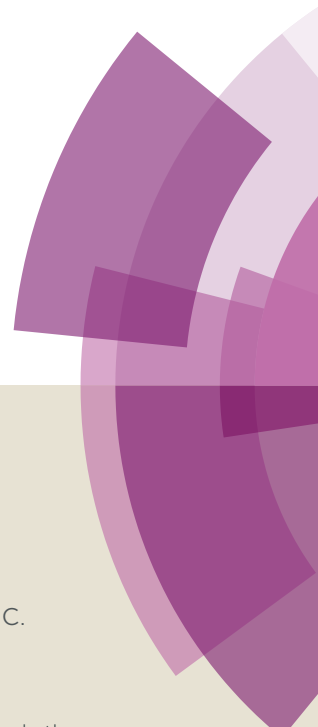
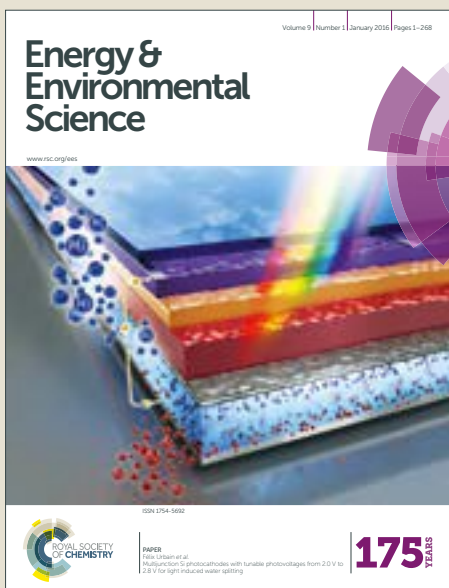


Energy & Environmental Science

Accepted Manuscript



This article can be cited before page numbers have been issued, to do this please use: P. Tang, H. Xie, C. Ros, L. Han, M. Biset-Peiró, Y. He, W. Kramer, A. Perez-Rodriguez, E. Saucedo, J. Galan-Mascaros, T. Andreu, J. R. Morante and J. Arbiol, *Energy Environ. Sci.*, 2017, DOI: 10.1039/C7EE01475A.



This is an Accepted Manuscript, which has been through the Royal Society of Chemistry peer review process and has been accepted for publication.

Accepted Manuscripts are published online shortly after acceptance, before technical editing, formatting and proof reading. Using this free service, authors can make their results available to the community, in citable form, before we publish the edited article. We will replace this Accepted Manuscript with the edited and formatted Advance Article as soon as it is available.

You can find more information about Accepted Manuscripts in the [author guidelines](#).

Please note that technical editing may introduce minor changes to the text and/or graphics, which may alter content. The journal's standard [Terms & Conditions](#) and the ethical guidelines, outlined in our [author and reviewer resource centre](#), still apply. In no event shall the Royal Society of Chemistry be held responsible for any errors or omissions in this Accepted Manuscript or any consequences arising from the use of any information it contains.

Energy & Environmental Science

ARTICLE

Received 00th January 20xx,
Accepted 00th January 20xx

DOI: 10.1039/x0xx00000x

www.rsc.org/

Enhanced Photoelectrochemical Water Splitting of Hematite Multilayer Nanowires Photoanode with Tuning Surface State via Bottom-up Interfacial Engineering

PengYi Tang,^{a,b} HaiBing Xie,^a Carles Ros,^a LiJuan Han,^c Martí Biset-Peiró,^a YongMin He,^d Wesley Kramer,^e Alejandro Pérez Rodríguez,^a Edgardo Saucedo,^a José Ramón Galán-Mascarós,^{c,f} Teresa Andreu,^a Joan Ramon Morante,^a Jordi Arbiol^{b,f,*}

The optimization of multiple interfaces in hematite ($\alpha\text{-Fe}_2\text{O}_3$) based composites for photoelectrochemical water splitting to facilitate charge transport in the bulk, is of paramount importance to obtain enhanced solar-to-fuel efficiency. Herein, we report the fabrication of ITO/ $\text{Fe}_2\text{O}_3/\text{Fe}_2\text{TiO}_5/\text{FeNiOOH}$ multi-layer nanowires and a series of systematic experiments designed to elucidate the mechanism underlying the interfacial coupling effect of the quaternary hematite composite. The hierarchical ITO/ $\text{Fe}_2\text{O}_3/\text{Fe}_2\text{TiO}_5/\text{FeNiOOH}$ nanowires display photocurrents more than an order of magnitude greater than pristine Fe_2O_3 nanowires (from 0.205 mA cm^{-2} to 2.2 mA cm^{-2} at 1.23 V vs RHE and 1 sun), and are higher than most of recently reported state-of-the-art hematite composites. Structural, compositional and electrochemical investigations disclose that the surface states (SS) are finely regulated via the atomic addition of an Fe_2TiO_5 layer and FeNiOOH nanodots, while the upgrading of back contact conductivity and charge donor densities originate from the epitaxial relationship and enhanced Sn doping contributed from ITO underlayer. We attribute the superior water oxidation performance to the interfacial coupling effect of ITO underlayer (Sn doping and back contact conductivity promoter), atomic level Fe_2TiO_5 coating (Ti doping, surface state density and energy level modulation) and FeNiOOH nanodots eletrocatalyst (regulating surface state energy level). Our work suggests an effective pathway for rational designing highly active and cost-effective integrated photoanodes for photoelectrochemical water splitting.

1. Introduction

Hematite based photoanodes have been intensively investigated on account of several promising properties which make it a potential candidate as a water splitting photoanode. Hematite materials are low cost, and environmentally-friendly owing to its high natural abundance. More importantly, in terms of its applications in PEC, hematite possesses high photo-chemical stability, a narrow bandgap (1.9–2.2 eV), and a theoretical maximum solar-to-hydrogen (STH) efficiency of 15.4 %, corresponding to 12.5 mA cm^{-2} at Air-Mass 1.5 Global solar illumination, which exceeds the STH

benchmark efficiency of 10% required for practical applications.^{1–2} However, its relatively low absorption coefficient, short excited-state lifetime (10^{-6} s),^{3–4} poor oxygen evolution reaction kinetics, short hole diffusion length, and poor electrical conductivity leads to multiple electron-hole recombination pathways occurring in the bulk, interfaces, and surfaces and significantly limits the photoelectrochemical (PEC) activity of hematite.² As a rapid charge transport and transfer between the back substrate, photoactive semiconductor, the catalyst and electrolyte is necessary for efficient STH performance, the electronic and structural properties of back substrate/semiconductor/catalyst/electrolyte interfaces play a vital role in PEC performance.^{5–10} The electron-hole recombination at the interface of the back substrate and hematite is critical for the electron transport from bulk hematite to the current collector and thus affects the overall PEC photocurrent response.^{2, 9, 11–14} For instance, Zheng et al. reported an integrated hematite, TiO_x and FeOOH photoanode and obtained a photocurrent around 1.5 mA cm^{-2} , which is still much lower than the theoretical value (12.5 mA cm^{-2}) of hematite.¹² Even though this design simultaneously reduces charge recombination in the bulk and surface of hematite, the obtained photocurrent response suffers from intensive back electron-hole recombination between hematite nanowires and FTO substrate. This phenomenon is likely derived from the Sn loss in FTO substrate during the high temperature (1000°C) sintering treatment which leads to poor electron conductivity in the back

^a Catalonia Institute for Energy Research (IREC), Jardins de les Dones de Negre 1, Sant Adrià del Besòs, Barcelona 08930, Catalonia, Spain.

^b Catalan Institute of Nanoscience and Nanotechnology (ICN2), CSIC and The Barcelona Institute of Science and Technology (BIST), Campus UAB, Bellaterra, 08193 Barcelona, Catalonia, Spain. *Email: arbiol@icrea.cat

^c Institute of Chemical Research of Catalonia (ICIQ), The Barcelona Institute of Science and Technology (BIST), Avinguda Països Catalans 16, Tarragona 43007, Catalonia, Spain.

^d School of Physical Science and Technology, Lanzhou University, Lanzhou 730000, China.

^e Beckman Institute and Division of Chemistry and Chemical Engineering, California Institute of Technology, 1200 East California Boulevard, Pasadena, California 91125, United States.

^f ICREA, Pg. Lluís Companys 23, 08010 Barcelona, Catalonia, Spain.

† Electronic Supplementary Information (ESI) available: XRD, UV-Vis spectrum, SEM, EDS, TEM, STEM-EELS maps, PEC characteristics, PEIS, Equivalent circuit, Mott-Schottky plots, XPS spectra and crystal model. See DOI: 10.1039/x0xx00000x

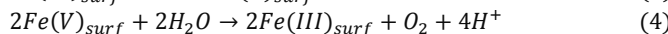
ARTICLE

Energy & Environmental Science

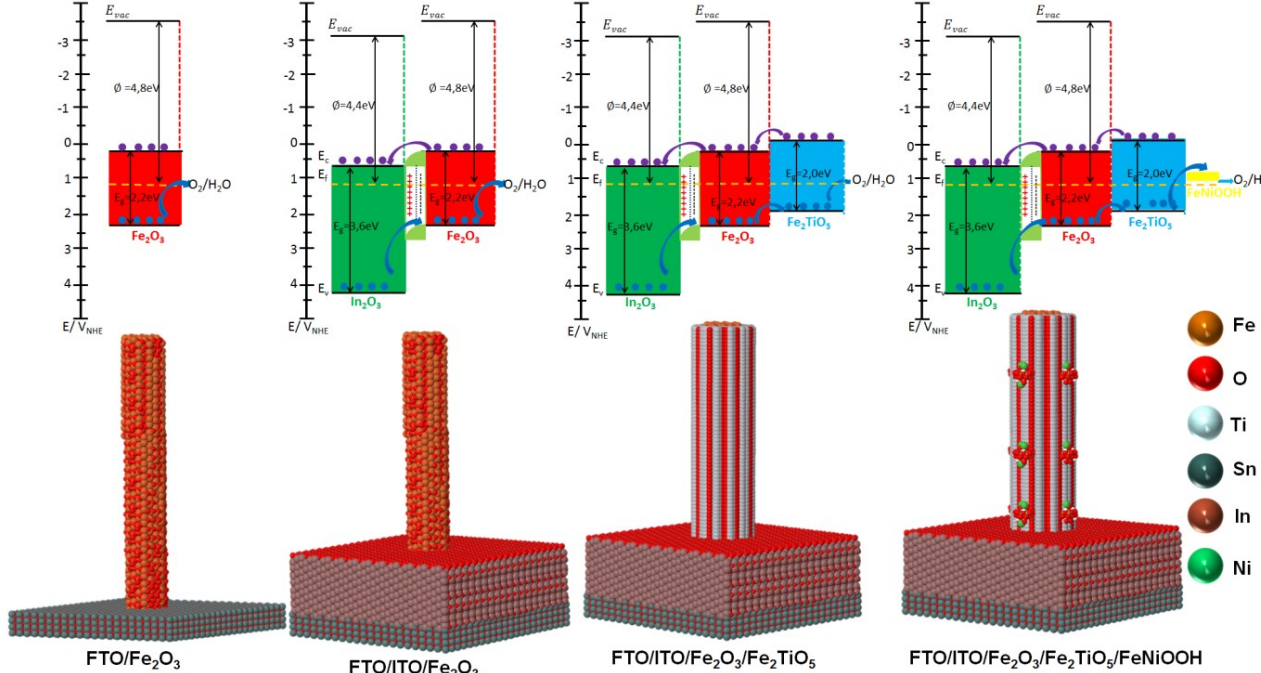
contact.¹³⁻¹⁴ Therefore, it is essential to optimize the back interface of the FTO substrate and hematite. This may be accomplished by introducing a conductive buffer layer, such as an ITO underlayer between hematite and the FTO substrate. Moreover, the energetic and electronic structure of hematite can be tuned by forming an advantageous heterojunction interface, which can reduce the charge recombination at the semiconductor junction interface and thus facilitates hole transport to the electrolyte for oxygen evolution reaction (OER).^{10, 12} Recently, we prepared mesoporous hematite- Fe_2TiO_5 heterojunction film, with an optimized 10% TiO_2 doping, which possessed a 15-fold photocurrent increment (up to 1.3 mA cm⁻² at 1.23 V vs RHE).¹⁰ Furthermore, iron-nickel oxide hydroxides (FeNiOOH) have attracted widespread attention as oxygen evolution catalysts (OEC) due to their unique structure and good OER activity in alkaline medium, whose OER activity can be adjusted according to film thickness.¹⁵⁻¹⁷ Coupling FeNiOOH OEC on hematite photoanodes is supposed to effectively suppress the electron-hole pair recombination and accelerate reaction kinetics at the photoactive semiconductor/electrolyte interface (SEI).¹⁸⁻¹⁹ In light of this, it is thereby of high interest to design an integrated quaternary multilayer photoanode with a high electrical conductive underlayer (ITO layer, to protect against Sn loss from the FTO substrate), an advantageous heterojunction ($\text{Fe}_2\text{O}_3/\text{Fe}_2\text{TiO}_5$),¹⁰ and an efficient OEC layer (FeNiOOH) to simultaneously reduce the interfacial, bulk and surface charge recombination as well as to enhance its PEC performance.

On the other hand, the kinetic process of water oxidation at SEI^{10, 20-22} and the identification of the active sites²³⁻²⁵ for water splitting

have drawn the attention of many researchers. L. M. Peter et al. employed photoelectrochemical impedance spectroscopy (PEIS) for the kinetic analysis of the multistep water oxidation reaction and proposed that OER in hematite involves high-valent iron states formed at the surface.²⁰ The water oxidation on hematite surface is a 4-electron process, which occurs following the equations (1-4), with the holes being 'stored' in the Fe(IV) and Fe(V) intermediate states.²⁰



T. Hamann et al. illustrated a general physical model and systematically discussed the suitable equivalent circuit for illustrating the EIS data for the hematite electrode, including surface states (SS) at the SEI where holes accumulate.²¹ Most recently, T. Hamann et al. investigated the water-oxidation reaction on hematite via in-situ infrared spectroscopy; and the existence of $\text{Fe}^{IV}=\text{O}$ group (an intermediate in the PEC water oxidation reaction) has been directly observed, which is the origin of the presence of hematite surface states.²⁶ Moreover, our previous investigation has proposed a charge transfer mechanism through hole trapping at surface state and its isoenergetic transfer to water for hematite/ Fe_2TiO_5 composite system and demonstrated that the surface state density of hematite can be tuned by controlling the amount of TiO_2 .¹⁰ In addition, it is well established that SS exist due to the termination of lattice periodicity at the species' surface, and the unpaired electrons in the dangling bonds of surface atoms



Schematic 1. Top: Thermodynamic scheme for the charge transfer processes at 1.23 V vs. RHE of SEI under illumination for Fe_2O_3 , ITO/ Fe_2O_3 , ITO/ $\text{Fe}_2\text{O}_3/\text{Fe}_2\text{TiO}_5$, and ITO/ $\text{Fe}_2\text{O}_3/\text{Fe}_2\text{TiO}_5/\text{FeNiOOH}$ electrodes. The black arrows indicate the bandgap of In_2O_3 (ITO matrix), hematite and Fe_2TiO_5 . The dark blue arrow refers to the hole transfer process at the heterojunction interfaces. The purple arrow refers to the electron transfer process present at the heterojunction interfaces. For simplicity, interfacial charge transfer is considered to occur through the E_V and/or E_C states directly, without the intervention of interfacial SS. In all photoanodes, 4 electron-hole couples per visible active semiconductor are depicted. In_2O_3 (main ingredient of ITO matrix): green; Fe_2O_3 : red; Fe_2TiO_5 : indigo; FeNiOOH : yellow. Bottom: the atomic supercell models illustrate the interfaces existing at In_2O_3 (ITO matrix), hematite, Fe_2TiO_5 and FeNiOOH species in the integrated electrodes.

interact with each other forming an electronic state with a narrow energy band (mid band) at the semiconductor band gap.²⁷⁻²⁸ In this regard, we propose that, by integrating the hematite nanowires with an ITO underlayer, Fe_2TiO_5 and FeNiOOH coating layers steply, the SS would be finely regulated because the chemical environment of $\text{Fe}^{IV}=\text{O}$ present at SEI will vary slightly during the water oxidation process.²⁹⁻³²

2. Results

Based on the wealth of reported band gap information for In_2O_3 , hematite, Fe_2TiO_5 and FeNiOOH ,^{10, 33} a type II band alignment composed of multiple ITO/hematite/ Fe_2TiO_5 / FeNiOOH interfaces can be constructed via gradual incorporation of ITO, Fe_2TiO_5 and FeNiOOH layers in hematite nanowires.^{27, 34} As illustrated in Schematic 1, upon light illumination, the pristine Fe_2O_3 electrode suffers from a large recombination rate that yields a low photocurrent, as holes are sluggishly transferred to water. For ITO/ Fe_2O_3 electrode, since both In_2O_3 and hematite are n-type semiconductors with different work functions, a heterojunction with a potential barrier will form at their interface. In_2O_3 (main ingredient of ITO) has a lower work function compared to hematite, thus the electrons in the Fermi level (E_f) of In_2O_3 will migrate to E_f of Fe_2O_3 until their E_f equalized.³³ At the equilibrium state, an electron depletion layer (marked as double layer charge between hematite and In_2O_3) will be generated at the heterojunction interface and thus a built-in electron field will be formed, which will accelerate the separation of photo-generated charge carriers and reduce the recombination rate and thus result in enhanced photocurrent.^{27,35} Since Fe_2TiO_5 and hematite's relative conduction band (CB) and valence band (VB) edge positions enable a cascade of charge migration, holes are transferred from Fe_2O_3 to Fe_2TiO_5 and conversely electrons are transferred from Fe_2TiO_5 to Fe_2O_3 in a conveyor belt fashion.¹⁰ Upon coating of ultrathin Fe_2TiO_5 onto ITO/ Fe_2O_3 nanowires, the hematite nanowires can accommodate the ultrathin pseudobrookite phase shell at the surface, forming the advantageous $\text{Fe}_2\text{O}_3/\text{Fe}_2\text{TiO}_5$ heterojunction. The heterojunctions in the ITO/ $\text{Fe}_2\text{O}_3/\text{Fe}_2\text{TiO}_5$ electrode reduces the grain boundary recombination by preventing charge accumulation in the nanowires and at the interfaces, thus is expected to further enhance the photocurrent response. Finally, there is consensus that, coupling FeNiOOH on photoanodes effectively suppresses the charge recombination and accelerates reaction kinetics at the SEI.³⁶⁻⁴² The deposition of FeNiOOH onto the ITO/ $\text{Fe}_2\text{O}_3/\text{Fe}_2\text{TiO}_5$ nanowires should further increase the surface work function, resulting in a remarkable enhancement of the barrier height and built-in electric field for the migration of photogenerated holes to the electrode surface.³⁶⁻³⁸ With this in mind, an ITO/hematite/ $\text{Fe}_2\text{TiO}_5/\text{FeNiOOH}$ heterojunction nanowire was designed and fabricated via a combination of sputtering, hydrothermal, ALD and photoelectrochemical deposition techniques, as displayed in Schematic 2.

2.1) XPS spectrum

The surface electronic states and composition of each electrode were analysed by XPS and all binding energies were corrected for samples charging effect regarding the C 1s line at 284.6 eV. Figure 1 and Figure S1 present the Sn 3d, O 1s, Fe 2p, In 3d, Ti 2p and Ni 2p core level XPS scans at higher resolution over smaller energy

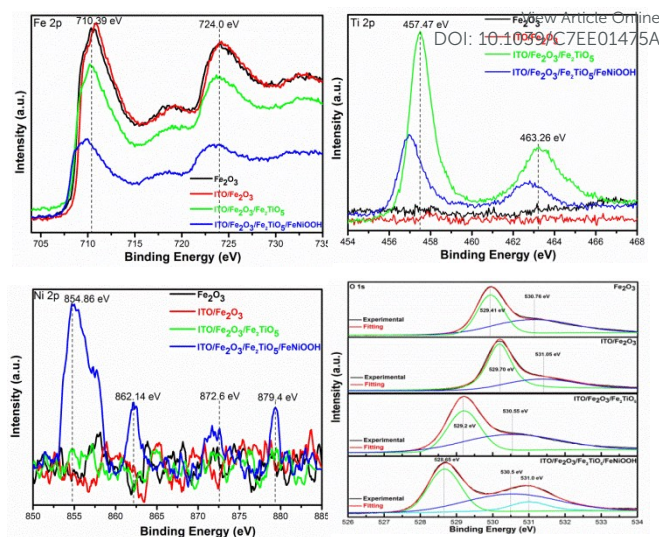


Figure 1. High resolution XPS spectra of Fe 2p, Ti 2p, Ni 2p and O 1s, from the Fe_2O_3 , ITO/ Fe_2O_3 , ITO/ $\text{Fe}_2\text{O}_3/\text{Fe}_2\text{TiO}_5$, and ITO/ $\text{Fe}_2\text{O}_3/\text{Fe}_2\text{TiO}_5/\text{FeNiOOH}$ electrodes.

windows. The Fe 2p_{1/2} and 2p_{3/2} peaks at the binding energies of 710.39 eV and 724.00 eV confirm the presence of the Fe element in these four electrodes. Additionally, two satellite peaks of the Fe 2p main line are at approximately 8.1–8.5 eV lower energy than the main line, indicating the presence of Fe^{3+} species.^{10, 43} A positive shift of the Fe peaks after the sputtering of ITO under layer reflects a decrease in the electron density of the Fe_2O_3 due to electron transfer from Fe_2O_3 to ITO layer. Conversely, a negative shift of the Fe peak is detected after the deposition of Fe_2TiO_5 and FeNiOOH layers. These shifts can be ascribed to the surface binding interaction between ITO, Fe_2O_3 , Fe_2TiO_5 and FeNiOOH , which induces an electron transfer in the integrated photoanode following the order: $\text{FeNiOOH} \rightarrow \text{Fe}_2\text{TiO}_5 \rightarrow \text{Fe}_2\text{O}_3 \rightarrow \text{ITO}$ as depicted in Schematic 1.⁴⁴ The Sn 3d_{3/2} and Sn 3d_{5/2} peaks (Figure S1) at 494.80 and 486.26 eV with splitting energy of 8.54 eV is consistent with reported values of Sn^{4+} .^{33,45} Furthermore, the In 2p_{1/2} and 2p_{3/2} core level XPS spectrum (Figure S1) has two weak, broad peaks around 451.60 and 444.76 eV, in good agreement with In_2O_3 .³³ Comparing with the strong intensity of Sn 3d peaks, the relative weak intensity of In 2p peaks means that the formation of In^{3+} ions is closer to the substrate, indicating that Sn doping dominates the Fe_2O_3 nanowires rather than In doping. The Ti 2p_{1/2} and 2p_{3/2} peaks at 463.26 and 457.27 eV reveal the successfully coating of Fe_2TiO_5 for ITO/ $\text{Fe}_2\text{O}_3/\text{Fe}_2\text{TiO}_5$ and ITO/ $\text{Fe}_2\text{O}_3/\text{Fe}_2\text{TiO}_5/\text{FeNiOOH}$ electrodes.¹⁰ Coinciding with the observed shift of Fe 2p peaks, after the FeNiOOH deposition, the Ti peaks shift to a negative binding energy direction, again implying electron transfers from the FeNiOOH to the Fe_2TiO_5 layer. Moreover, the presence of Ni in FeNiOOH was also investigated. The weak Ni 2p_{1/2} and 2p_{3/2} core level XPS peaks located at 872.60 eV and 854.86 eV and the associated satellite peaks at 862.14 eV and 879.40 eV are observed in the ITO/ $\text{Fe}_2\text{O}_3/\text{Fe}_2\text{TiO}_5/\text{FeNiOOH}$ electrode, confirming the presence of FeNiOOH .⁴⁴ The O 1s XPS spectrum of ITO/ $\text{Fe}_2\text{O}_3/\text{Fe}_2\text{TiO}_5/\text{FeNiOOH}$ electrode is composed by three peaks. The low binding energy at 529.41 eV and the higher binding energy component at 531.05 eV are attributed to the coordination of oxygen bounded to iron atoms from the Fe_2O_3 moiety and surface absorbed OH group, respectively.⁴⁶ The shift

ARTICLE

Energy & Environmental Science

behaviour of these two O 1s peaks of Fe_2O_3 is in accordance with shifts observed for the Fe 2p and Ti 2p peaks. Whereas, the 531.00 eV O1s peak can be assigned to the OOH bonding likely to the FeNiOOH species.⁴⁴ The consistent shifts in the binding energy observed in the XPS data for these electrodes indicate charge transfer processes that benefit electron-hole separation, further supporting the well-constructed multiple ITO/hematite/ Fe_2TiO_5 / FeNiOOH heterojunction with type II band alignment.

2.2) Structural Characterization

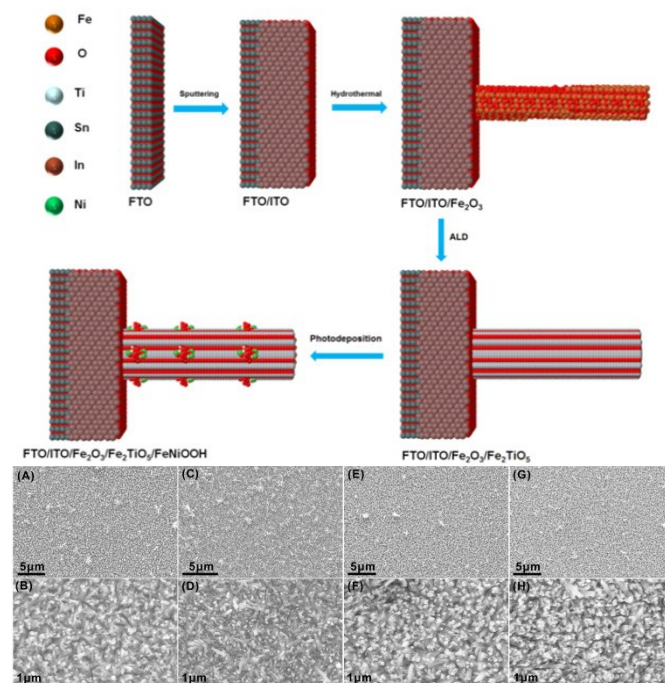


Figure 2. Top: Schematic 2. Atomic supercell model illustration of the synthetic procedure for ITO/ $\text{Fe}_2\text{O}_3/\text{Fe}_2\text{TiO}_5/\text{FeNiOOH}$ integrated photoanodes. Bottom: SEM images (top view) of Fe_2O_3 (A, B), ITO/ Fe_2O_3 (C, D), ITO/ $\text{Fe}_2\text{O}_3/\text{Fe}_2\text{TiO}_5$ (E, F), and ITO/ $\text{Fe}_2\text{O}_3/\text{Fe}_2\text{TiO}_5/\text{FeNiOOH}$ (G, H) electrodes.

The morphology and crystal phase evolution of these electrodes were monitored by SEM, EDS, XRD, TEM and STEM-EELS maps. Vertically aligned Fe_2O_3 nanowires were grown on a FTO or 105 nm ITO coated FTO substrate (the corresponding SEM images of these two substrates are displayed in Figure S18) via a previously reported hydrothermal method.⁴⁷ The Fe_2O_3 nanowires have a diameter range from 50 to 100 nm (Figure 2A, B and Figure 2C, D). Subsequently, an ultrathin TiO_2 layer was coated onto ITO/ Fe_2O_3 nanowires by ALD (30 cycles). The surface TiO_2 was subsequently transformed into Fe_2TiO_5 through a post-quenching process in atmosphere at 750 °C for 30 min. As displayed in Figure 2E and F, the Fe_2TiO_5 coating onto ITO/ Fe_2O_3 is homogeneous with no change in the nanowires configuration. Interestingly, the ITO/ $\text{Fe}_2\text{O}_3/\text{Fe}_2\text{TiO}_5$ nanowires appear to be straighter than the ITO/ Fe_2O_3 nanowires, this is likely due to the confinement effect from the ultrathin Fe_2TiO_5 layer (This phenomenon is similar to the function of SiO_2 in the fabrication of mesoporous Fe_2O_3 reported by K. Sivula et al.).⁴⁸ When 10 mC FeNiOOH were further photo-electrodeposited onto the ITO/ $\text{Fe}_2\text{O}_3/\text{Fe}_2\text{TiO}_5$ nanowires, no visible nanostructure could be observed on the nanowires surface (Figure 2G and H), indicating its

ultrathin configuration. The crystal phase and elemental information were characterized by XRD (Figure S2A) and EDS (Figure S3), confirming the presence of In_2O_3 , hematite, pseudobrookite and FeNiOOH in the corresponding electrodes.

To identify each crystal phases via HRTEM and probe the spatial distribution of these components in the integrated electrodes, we created crystal models based on the single crystal data in the Inorganic Crystal Structure Database (ICSD), as displayed in Figure S4. With these crystal models, the diffraction patterns visualized from different zone axis of each phase can be simulated. Then, the simulated diffraction pattern is compared with the power spectrum (FFT) obtained on the atomic resolution HRTEM experimental images for the identification of the crystal phases in the composite electrodes. Figure S5 shows low magnification TEM images of the Fe_2O_3 electrode with nanowire-like morphology, while its HRTEM and detailed atomic structure are displayed in Figure 3A. The corresponding temperature coloured power spectrum (Figure 3A right) indicates that the structure corresponds to the trigonal Fe_2O_3 , [R3-CH]-Space group 167, also known as hematite, with lattice parameters of $a = b = 0.50342$ nm, $c = 1.37483$ nm, and $\alpha = \beta = 90^\circ$ and $\gamma = 120^\circ$ as visualized along the [21-2] direction. The HRTEM and atomic structure detail of the ITO/ Fe_2O_3 electrode in Figure 3B demonstrate that the modification of FTO substrate with 105 nm ITO underlayer does not alter the crystal phase of Fe_2O_3 nanowires. The temperature coloured power spectrum (right of Figure 3B) of ITO/ Fe_2O_3 electrodes indicates that the nanowires retain their single crystal hematite nature as visualized along the [110] direction, this is further supported by Figures S6 and S7. Figure 3C (left) shows the HRTEM image of the edge region of a single ITO/ $\text{Fe}_2\text{O}_3/\text{Fe}_2\text{TiO}_5$ nanowire extracted from the ITO/ $\text{Fe}_2\text{O}_3/\text{Fe}_2\text{TiO}_5$ electrode nanowire array. The corresponding power spectrum (Figure 3C right) shows that the nanowire is composed of a hematite core (Fe_2O_3) and a Fe_2TiO_5 shell ([BBMM]-Space group 63, with lattice parameters of $a = 0.9793$ nm, $b = 0.9979$ nm, $c = 0.3732$ nm, and $\alpha = \beta = \gamma = 90^\circ$), as visualized along the [42-1] and [001] directions, respectively. RGB coloured phase filtered images corresponding to the selected area of ITO/ $\text{Fe}_2\text{O}_3/\text{Fe}_2\text{TiO}_5$ electrode in Figure 3C are exhibited on the right. Figures S8 and S9 clearly confirm the homogenous coating of the Fe_2TiO_5 layer on the surface of the Fe_2O_3 nanowires. Moreover, the atomic density profile in the inset of the left HRTEM image in Figure 3C, reveals that the thickness of the Fe_2TiO_5 shell is 0.78 ± 0.02 nm thick, in agreement with the estimated 0.81 nm from the ALD process. Figure 3D displays a HRTEM image (left) of the electrode after the deposition of FeNiOOH to form the quaternary ITO/ $\text{Fe}_2\text{O}_3/\text{Fe}_2\text{TiO}_5/\text{FeNiOOH}$ structure. The presence of hematite and pseudobrookite phases was identified by their power spectrum (Figure 3D middle). It is noteworthy that the crystal diffraction spots of FeNiOOH , while visible, are weak showing few crystallites (low magnification TEM images are displayed in Figure S10), consistent with the XRD results indicating that it is primarily amorphous.^{44,49-52} Moreover, the corresponding RGB phase filtered image (Figure 3D right) illustrates the localized presence of hematite (nanowire core), pseudobrookite (shell) and FeNiOOH nanodot (surface crystallite in blue, showing a 0.256 nm plane distance corresponding to its (021) plane).⁵²⁻⁵⁵

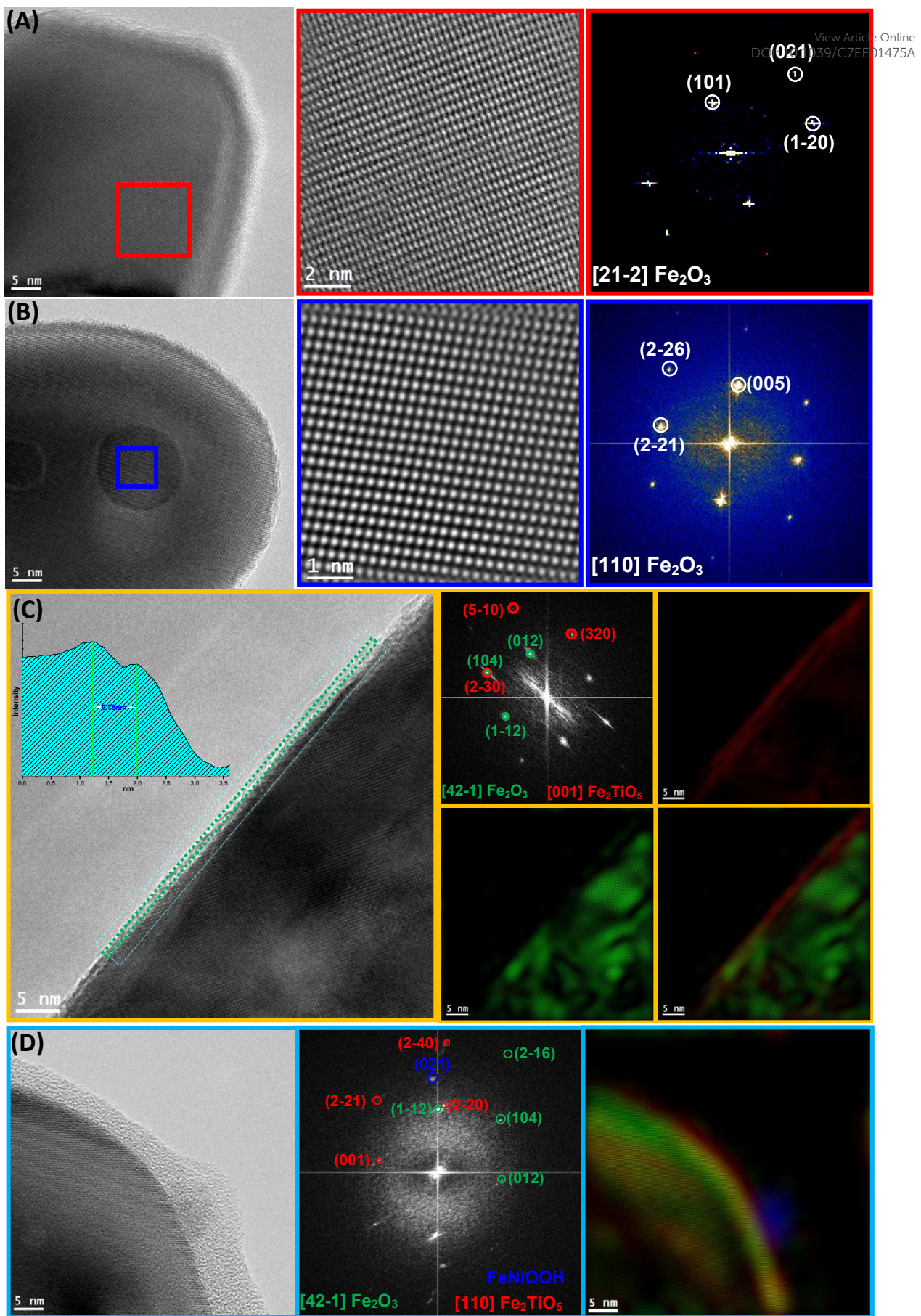


Figure 3. HRTEM, power spectrum and RGB coloured phase filtered structural images of the Fe_2O_3 (A), ITO/ Fe_2O_3 (B), ITO/ $\text{Fe}_2\text{O}_3/\text{Fe}_2\text{TiO}_5$ (C) and ITO/ $\text{Fe}_2\text{O}_3/\text{Fe}_2\text{TiO}_5/\text{FeNiOOH}$ (D) electrodes.

ARTICLE

Energy & Environmental Science

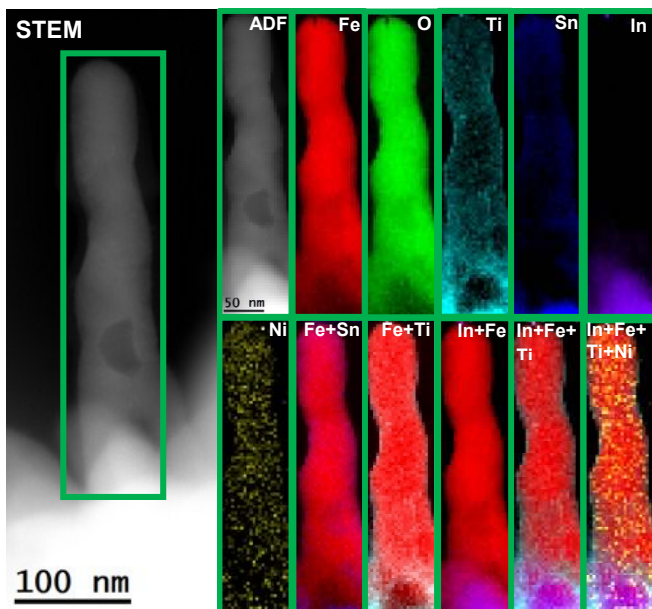


Figure 4: EELS chemical composition maps obtained from the green rectangled area on the ADF-STEM micrograph selected on one of the nanowires extracted from the ITO/Fe₂O₃/Fe₂TiO₅/FeNiOOH electrode sample. Individual Fe (red), O (green), Sn (blue), In (purple), Ti (indigo) and Ni (yellow) maps and their RGB composite.

The chemical composition of the interfaces in the ITO/Fe₂O₃/Fe₂TiO₅/FeNiOOH electrodes, were investigated by EELS maps using the K edge for O, M edges for In, Sn, and the L edges for Fe, Ti and Ni. The STEM-EELS composition maps of Fe₂O₃ (Figures S11-S12), ITO/Fe₂O₃ (Figures S13-S14) and ITO/Fe₂O₃/Fe₂TiO₅ (Figures S15-S16) electrodes are included in the Electronic Supplementary Information (ESI). As displayed in the STEM image of Figure 4, the Fe₂O₃/Fe₂TiO₅/FeNiOOH composite nanowire (green squared region) is grown directly onto the ITO matrix (brighter bottom region). The individual Fe, Sn and Fe+Sn RGB composite EELS maps in Figure 4 show that the Sn from ITO matrix diffuses into the hematite nanowires, revealing an intensive Sn doping throughout the ITO/Fe₂O₃/Fe₂TiO₅/FeNiOOH electrode as compared to weak Sn signal detected in the nanowires corresponding to the Fe₂O₃ electrode (Figures S11-S12). By contrast, In, in the form of In₂O₃, only present in the bottom region of the electrode corresponding to the ITO under layer, as supported by the individual In and O EELS mappings shown in Figure 4 and HRTEM result in Figure S6. Together with the STEM-EELS maps obtained in the ITO/Fe₂O₃ electrode (Figures S13-S14) and the ITO/Fe₂O₃/Fe₂TiO₅ electrode (Figures S15-S16), these data demonstrate that there is almost no In doping into the Fe₂O₃ nanowires upon the sputtering of the ITO under layer, which is consistent with the XPS result. The Fe, Ti and Fe+Ti RGB composite EELS elemental maps obtained on the ITO/Fe₂O₃/Fe₂TiO₅/FeNiOOH electrode (Figure 4) show complete coverage of the ultrathin Fe₂TiO₅ shell over the Fe₂O₃ nanowires. The individual Fe, Ni, O EELS elemental maps illustrate the presence of discontinuous distributed FeNiOOH species decorated on the nanowires, in good agreement with the nanodot-like FeNiOOH structure observed in Figure 3D, Figures S10 and S17. RGB composite EELS elemental maps of In+Fe, In+Fe+Ti and In+Fe+Ti+Ni together illustrate the successful construction of the quaternary

ITO/Fe₂O₃/Fe₂TiO₅/FeNiOOH heterojunction nanowires via step-wise incorporation of ITO, Fe₂O₃, Fe₂TiO₅ and FeNiOOH. [DOI: 10.1039/C7EE01475A](https://doi.org/10.1039/C7EE01475A)

2.3) PEC performance characterization

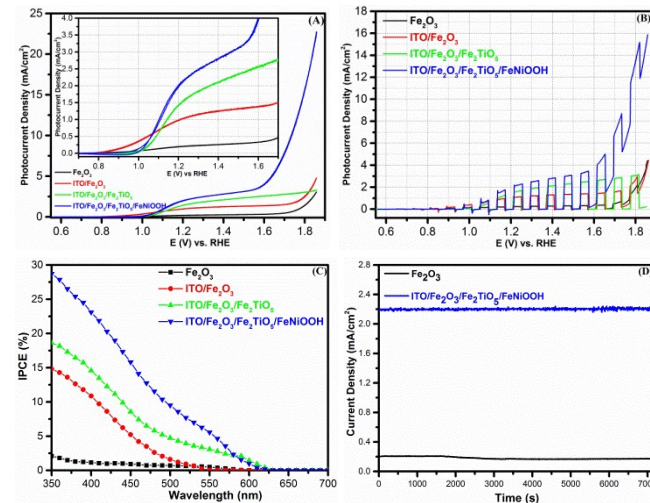


Figure 5. (A) Cyclic voltammetry (the inset shows its magnified plot), (B) chopped light photocurrent-potential curves, (C) IPCE and (D) photoelectrochemical stability test operated at 1.23 V vs RHE for the Fe₂O₃, ITO/Fe₂O₃, ITO/Fe₂O₃/Fe₂TiO₅, and ITO/Fe₂O₃/Fe₂TiO₅/FeNiOOH electrodes. All polarization potentials reported here are relative to the reversible hydrogen electrode (RHE), and current densities are per geometric area.

To determine the optimum conditions for the integration of ITO/Fe₂O₃/Fe₂TiO₅/FeNiOOH electrodes, different synthesis parameters, including ITO thickness, TiO₂ cycles, post-quench sintering conditions and FeNiOOH deposition charge, were examined (for details see supplementary Figures S18-S27 and associated discussions in the ESI). The PEC performance measured for the optimized four representative photoanodes is displayed in Figure 5. CVs of pristine Fe₂O₃ nanowires (Figure 5A) show a relatively low photo-response over the whole potential window with a photocurrent density of 0.205 mA cm⁻² at 1.23 V vs RHE, thermodynamic potential for OER. Upon introduction of the ITO underlayer, the photocurrent density increase to 1.05 mA cm⁻² at 1.23V vs RHE. The onset potential of ITO/Fe₂O₃ still remains at 0.85 V, which is the same as that of pristine Fe₂O₃ electrode. Besides, the CV curve of Fe₂O₃ and ITO/Fe₂O₃ electrodes at high potential region (over 1.7 V) exhibits the same trend, indicating the presence of similar Fe₂O₃|electrolyte interface.¹⁵ In contrast, the ITO/Fe₂O₃/Fe₂TiO₅ electrode exhibits an anodic shift in the onset potential to 1.0 V vs RHE, along with an increase in the photocurrent density to 1.56 mA cm⁻² at 1.23 V vs RHE. The positive shift in the onset potential upon coating Fe₂TiO₅ onto the hematite nanowires is consistent with the result reported by J. Zhong et al,⁵³ which is probably due to the suppressing of the surface state density at potential lower than 1.0 V vs RHE when compared with that of ITO/Fe₂O₃ electrode, as displayed in Figure 7A. While, the CV curve of ITO/Fe₂O₃/Fe₂TiO₅ electrodes at high potential region (over 1.7 V) is somehow suppressed compared with that of Fe₂O₃ and ITO/Fe₂O₃ electrodes, illustrating its SEI variation. Despite some improvement, the PEC performance for the ITO/Fe₂O₃/Fe₂TiO₅ nanowires remains unsatisfactory, likely caused by the slow water oxidation kinetics.⁵⁴ Thus, an optimized OEC (Figures S24-S25), 10 mC FeNiOOH was deposited on the surface of the ITO/Fe₂O₃/Fe₂TiO₅ nanowires. In the

case of ITO/Fe₂O₃/Fe₂TiO₅/FeNiOOH electrode, a cathodic shift in onset potential for OER to 0.95 V is observed relative to the ITO/Fe₂O₃/Fe₂TiO₅ electrode. Its photocurrent density of 2.2 mA cm⁻² at 1.23 V vs RHE represents the highest value among these four photoanodes, and is even higher than the photocurrent response of recently reported state-of-the-art Fe₂O₃ composite photoanodes (Table S2). The tremendous increment of the photocurrent at high potential region (over 1.6 V, dominated by the dark current response from OEC) implies the successfully combination of the merits of the photocatalytic activity of ITO/Fe₂O₃/Fe₂TiO₅ and the electrocatalytic activity of FeNiOOH.¹⁵ Besides, there is a photocurrent plateau for all electrodes, which is derived from the transition of hole acceptor from OH⁻ to water in the electrolyte according to the report of J.C. Zhao et al.²² Furthermore, transient photocurrent measurements, based on the CVs under chopped light illumination, were performed for each photoanode. As shown in Figure 5B, all electrodes exhibit a prompt and reproducible photocurrent response with respect to the irradiation signal ON-OFF cycles. The current density of these electrodes under illumination follows an ascending order as: Fe₂O₃ < ITO/Fe₂O₃ < ITO/Fe₂O₃/Fe₂TiO₅ < ITO/Fe₂O₃/Fe₂TiO₅/FeNiOOH photoanodes. This is in high accordance with the CV results and further demonstrates the enhancement in PEC performance provided by addition of ITO, Fe₂TiO₅ and FeNiOOH to hematite nanowires.

The incident photon-to-current conversion efficiency (IPCE) was measured to understand the relationship between the photocatalytic activity and light absorption. All samples exhibit photocatalytic activity in the visible light region (Figure 5C). Maximum IPCEs obtained at 350 nm, for Fe₂O₃, ITO/Fe₂O₃, ITO/Fe₂O₃/Fe₂TiO₅, and ITO/Fe₂O₃/Fe₂TiO₅/FeNiOOH photoanodes are 2.1%, 14.8%, 18.6%, and 28.7%, respectively. The large enhancement of IPCE for the ITO/Fe₂O₃/Fe₂TiO₅/FeNiOOH nanowires further supports the integrated coupling effect of ITO, Fe₂TiO₅ and FeNiOOH to the PEC performance. Additionally, the IPCE curves for all of these electrodes correlate with the UV-Vis absorption spectrum of Fe₂O₃ presented in Figure S2B, indicating that the Fe₂O₃ indeed acts as the sole visible light responsive semiconductor material. Thus, the enhanced PEC performance is preliminary attributed to a synergistic effect between ITO, Fe₂O₃, Fe₂TiO₅ and FeNiOOH rather than the primitively tandem function of each semiconductor material. The photoelectrochemical stability is operated by chronomperometric response at a constant applied working potential of 1.23 V vs RHE, as shown in Figure 5D. The photocurrent of Fe₂O₃ slightly decreases from 0.205 mA cm⁻² to 0.17 mA cm⁻² over the course of the 2h experiment. In contrast, no photocurrent degradation was observed for the ITO/Fe₂O₃/Fe₂TiO₅/FeNiOOH electrode during the stability test and maintained a photocurrent of 2.2 mA cm⁻² throughout.

2.4) PEIS and OER Mechanism investigations

All the above results illustrate that the incorporation of ITO, Fe₂TiO₅ and FeNiOOH largely improve the PEC performance of the hematite nanowires photoanode. Given that a physical model of the illuminated SEI for SS-mediated, indirect hole transfer has been well established and occurs in two consecutive steps: (i) hole trapping by SS, and (ii) hole transfer from SS to water molecules at the SEI.^{10, 23-}

²⁴ To gain further insight into the mechanism of this interfacial coupling effect, primary PEIS (Figure S28- S29) has been employed to identify the functions of the ITO, Fe₂O₃, Fe₂TiO₅ and FeNiOOH in the integrated ITO/Fe₂O₃/Fe₂TiO₅/FeNiOOH electrodes. PEIS measurements were performed at potentials, ranging from 0.65 V vs RHE (before the onset of photocurrent) to 1.36 V vs RHE (before the light-flux limited photocurrent region) because the effect of SS is more prevalent when unaffected by the light-flux limited and dark oxygen evolution factors.¹⁰ The obtained PEIS data was fitted based on the equivalent circuit displayed in the Schematic S1A.

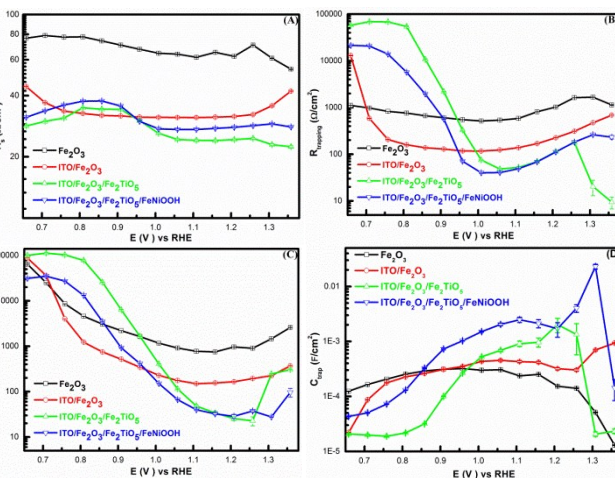


Figure 6. Equivalent circuit parameters obtained from fitting IS data for the Fe₂O₃, ITO/Fe₂O₃, ITO/Fe₂O₃/Fe₂TiO₅, and ITO/Fe₂O₃/Fe₂TiO₅/FeNiOOH electrodes in contact with 1M NaOH electrolytes under 1 sun illumination. R_s (A), R_{trap} (B), $R_{\text{ct,trap}}$ (C) and C_{trap} (D) as a function of the applied potential. R_s , resistance associated with the electric contacts of the electrode, electrolyte, etc. R_{trapping} , resistance associated with charge trapping at surface states. $R_{\text{ct,trap}}$, resistance associated with the charge transfer process from surface states. C_{trap} , capacitance associated with charge accumulation on the surface states.

Typically, the R_s , series resistance includes the resistance at the interface between the FTO substrate, or ITO underlayer, and Fe₂O₃ nanowires.^{9, 20} A substantial reduction in R_s is observed from ca. 70 Ωcm^{-2} for pristine Fe₂O₃ electrode to ca. 35 Ωcm^{-2} for composite Fe₂O₃ electrodes modified with the ITO underlayer, as displayed in Figure 6A. These results mean that the ITO underlayer is able to efficiently improve the back electrical contact and facilitate the electron transport from Fe₂O₃ to the FTO substrate. This improvement is attributed to the enhanced Sn doping in hematite nanowires¹³⁻¹⁴ and the epitaxial relationship between the Fe₂O₃ and In₂O₃ phases, as demonstrated by the HRTEM and STEM-EELS maps results. However, capacitance associated with charge accumulation in the bulk (C_{bulk} , Figure S30) was measured to be on the same order of magnitude for these electrodes with the exception of an abrupt peak at ca. 0.9 V for ITO/Fe₂O₃/Fe₂TiO₅, and ITO/Fe₂O₃/Fe₂TiO₅/FeNiOOH electrodes. It may be due to the addition of the ultrathin Fe₂TiO₅ shell, which slightly changes the electronic state of the electrodes.³⁵ Figure 6B shows the lowest value of the R_{trapping} for the ITO/Fe₂O₃/Fe₂TiO₅/FeNiOOH electrode as compared to the Fe₂O₃, ITO/Fe₂O₃ and ITO/Fe₂O₃/Fe₂TiO₅ electrodes at the potential window (0.9 V to 1.36 V).¹⁰ This is consistent with the correlation of a dip in the $R_{\text{ct,trap}}$ and a peak in the C_{trap} profile resulting in more efficient charge transfer kinetics during PEC.⁵⁵ Work by Hamann and coworkers,^{21, 56-57} suggest that a large C_{trap} and a low $R_{\text{ct,trap}}$ would

ARTICLE

Energy & Environmental Science

eventually render larger photocurrents, provided that the charge is transferred from SS to electrolyte. As shown in Figure 6C, for each of these four electrodes, a gradual decrease in $R_{ct,trap}$ is observed as the applied potential increases implying an increment of associated photocurrent response. Notably, the ITO/Fe₂O₃/Fe₂TiO₅/FeNiOOH photoanode possess a relative minimum $R_{ct,trap}$ from 0.9 V to 1.25 V, in line with the larger photocurrent variation at this region dominated by SS (Figure 5A). The $R_{ct,trap}$ at 1.25 V for ITO/Fe₂O₃/Fe₂TiO₅/FeNiOOH photoanode is ca. 34 times lower than that of the pristine Fe₂O₃ nanowires, further evidencing its best photocurrent response. While, the C_{bulk} (Figure S30) and C_{trap} (Figure 6D) show opposite tendencies. With the potential increase, the C_{bulk} decreases, whereas the C_{trap} increases, implying a larger percentage of charge located on SS; similarly, a relative optimum value (C_{trap}/C_{bulk} at 1.23 V vs RHE) is observed in the ITO/Fe₂O₃/Fe₂TiO₅/FeNiOOH electrode. Figure S32 and Table S1 reveal that the bulk donor density for the ITO/Fe₂O₃ electrode ($2.75E+19\text{ cm}^{-3}$) is 6 times higher than that for the pristine Fe₂O₃ electrode ($4.60E+18\text{ cm}^{-3}$). This effect is derived from the enhanced Sn doping in the hematite nanowires that result from the addition of the ITO underlayer (Figure S13-S14) and is in good agreement with the significantly improved photocurrent response of the ITO/Fe₂O₃ electrode.¹³⁻¹⁴ With the coating of the Fe₂TiO₅ onto the ITO/Fe₂O₃ electrode, the bulk donor density is further improved to $5.80E+19\text{ cm}^{-3}$, indicating that there may be a small amount of Ti doping in the Fe₂O₃ nanowires and thus additional photocurrent enhancement (1.56 mA cm^{-2}) observed for the ITO/Fe₂O₃/Fe₂TiO₅ electrode.¹⁰

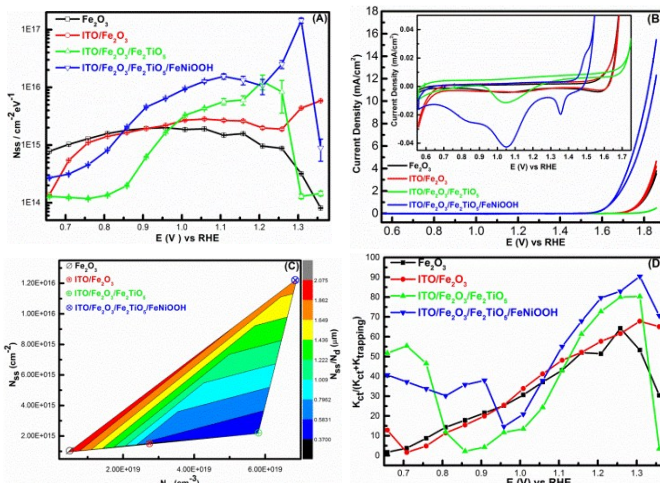


Figure 7. (A) Density of surface states (DOSS) as a function of the applied potential on the Fe₂O₃, ITO/Fe₂O₃, ITO/Fe₂O₃/Fe₂TiO₅, and ITO/Fe₂O₃/Fe₂TiO₅/FeNiOOH electrodes. Error bars stem from the goodness of the EIS data fittings. (B) CV curves scanned in dark at 20 mV s⁻¹ immediately after holding the electrode potential at 1.85 V vs. RHE. for 1 min under illumination of Fe₂O₃, ITO/Fe₂O₃, ITO/Fe₂O₃/Fe₂TiO₅, and ITO/Fe₂O₃/Fe₂TiO₅/FeNiOOH electrodes. (The inset shows its magnified plot). (C) Total surface state density (N_{ss}), donor density (N_d), and their ratio (N_{ss}/N_d) of Fe₂O₃, ITO/Fe₂O₃, ITO/Fe₂O₃/Fe₂TiO₅, and ITO/Fe₂O₃/Fe₂TiO₅/FeNiOOH electrodes. N_d was estimated from the slopes of the Mott-Schottky plots in the dark (Figure S31), whereas N_{ss} was obtained from integration of DOSS profiles (Figure 7A). Colour bar with a unit of μm is plotted at right Y axis for N_{ss}/N_d. (D) Ratio of the charge transfer rate constant (k_{ct}) and the sum of k_{ct} and trapping rate constant (k_{trapping}) at different potential, calculated with equation (6).

The general behaviour of the integrated multi-layer nanowires has been interpreted and phenomenologically correlated with the SS^{10,21,59} a deeper investigation of the photo-induced processes (i.e. charge generation and the subsequent transport to and transfer from the interfaces) is required to elucidate the interfacial charge transfer mechanism. In order to highlight the role of SS in the interfacial charge transfer process, we calculated the values for their density of surface states (DOSS) from the C_{trap} using equation (5):^{10,21}

$$N_{SS}(E) = C_{trap}(E)/q \quad (5)$$

Where N_{SS}(E) is the DOSS ($\text{cm}^{-2}\text{ eV}^{-1}$) as a function of applied potential and q is the electron charge ($1.602 \times 10^{-19}\text{ C}$). As shown in Figure 7A, it is possible to observe the SS energy distribution located below the photocurrent onset with its Fermi level pinned at SS.²¹

Our previous report¹⁰ has demonstrated that there is a direct correlation between the percentage of available filled surface states (larger DOSS) near the thermodynamic potential for OER, and the observed photocurrent response at 1.23 V vs RHE due to the required isoenergetic hole transfer process at the SEI.^{21,58} As displayed in Figure 7A, the N_{ss} of the four photoanodes follows the order: Fe₂O₃<ITO/Fe₂O₃<ITO/Fe₂O₃/Fe₂TiO₅<ITO/Fe₂O₃/Fe₂TiO₅/FeNiOOH across the entire SS dominated region (0.9 V to 1.36 V). The extended SS distribution from 0.65 V to 1.36 V in Fe₂O₃ and ITO/Fe₂O₃ electrodes probably spans inside the CB and triggers a deleterious Fermi level pinning at SS, which could be responsible for their relatively low photocurrent response. Moreover, the potential of the DOSS peak for the photoanodes shifts to more positive values, e.g., 0.9 V, 0.95 V, 1.25 V for the Fe₂O₃, ITO/Fe₂O₃, ITO/Fe₂O₃/Fe₂TiO₅ electrodes, respectively. Interestingly, the DOSS curve for the ITO/Fe₂O₃/Fe₂TiO₅/FeNiOOH electrode displays two peaks located at ca. 1.1 V and 1.3 V. This peak splitting phenomenon displayed by the ITO/Fe₂O₃/Fe₂TiO₅/FeNiOOH photoanode was further investigated by obtaining the CV curves scanned in the cathodic direction in dark at 20 mV s⁻¹ of these electrodes immediately after holding the electrode potential at 1.85 V vs. RHE. for 1 min under illumination to photoelectrochemically oxidize the surface states.^{26,29,59} As displayed in Figure 7B, for the ITO/Fe₂O₃/Fe₂TiO₅/FeNiOOH electrode, two cathodic peaks appear at around 1.05 V and 1.35 V, which is relatively consistent with the DOSS peaks position for the ITO/Fe₂O₃/Fe₂TiO₅/FeNiOOH electrode. Besides, T. Hamann et al. has quantitatively correlated the C_{trap} measured by both cyclic voltammetry and impedance spectroscopy with the absorption peak at 572 nm via operando UV-vis experiments, corresponding to the formation of Fe (IV) intermediate.²⁹ The splitting of one C_{trap} peak into two C_{trap} peaks were also observed upon ultra-thin ALD aluminium layer onto the hematite film, which is derived from the insufficient covering of aluminium overlayer and partial exposure of the hematite film.²⁹ Moreover, H. Irie et al. conducted preliminary in-situ UV-vis absorption spectra of FeNiOOH; and the incorporation of Fe into the NiOOH was found to induce an increase in absorption peak similar to that observed for hematite electrode, demonstrating the formation of an Fe(IV) intermediate in the FeNiOOH during the electrochemical test.³⁰ In our case, the DOSS peak splitting performance of the ITO/Fe₂O₃/Fe₂TiO₅/FeNiOOH electrode can be attributed to the incomplete coverage of FeNiOOH nanodots on the

nanowire surface in a manner consistent with the aluminium coated hematite reported by T. Hamann et al.²⁹ The peak located at 1.1 V vs RHE likely arises from Fe^{IV}=O surface intermediates on partially exposed Fe₂TiO₅ coating,³¹ as the same DOSS peak is observed for the ITO/Fe₂O₃/Fe₂TiO₅ electrode. The DOSS peak located at 1.3 V can then be assigned to the Fe^{IV}=O intermediates localized on the discontinuously distributed FeNiOOH nanodots.³⁰ In brief, the atomic level of Fe₂TiO₅ and FeNiOOH nanodots coatings can regulate the surface state density and energy level of hematite nanowires, which is probably attributed to the chemical environment variation of Fe^{IV}=O intermediates. After all, the identification of OER active sites in the integrated hematite photoanode⁶⁰ and further insights about the evolution of Fe^{IV}=O intermediates in these electrodes will need in-situ TEM experiments,⁶¹ which is beyond the scope of this work.

A combined comparison of the N_{ss}, N_d and N_{ss}/N_d ratio are presented in Figure 7C and Table S1. A large N_{ss}/N_d ratio does not ensure a good photoactivity because the number of donors in the hematite nanowires may not be high enough to endue the nanowires with good conductivity. This is demonstrated by the pristine Fe₂O₃ electrode which displays a high N_{ss}/N_d ratio but poor PEC performance. In stark contrast, ITO/Fe₂O₃ and ITO/Fe₂O₃/Fe₂TiO₅ electrodes display a relatively low N_{ss}/N_d ratio which possess enough donors in the nanowires to provide good conductivity, but a lack of surface reactive sites still limit the PEC performance of these electrodes. In the case of ITO/Fe₂O₃/Fe₂TiO₅/FeNiOOH electrode, a relatively high N_{ss}/N_d ratio corresponds to scenario in which N_{ss} and N_d are both numerous enough to give a larger photocurrent response. In addition, the charge transfer efficiency at the SEI is estimated through (equation (6)):^{10, 20}

$$\text{Transfer efficiency}(\%) = \frac{k_{ct}}{k_{ct} + k_{\text{trapping}}} = \frac{R_{\text{trapping}}}{R_{\text{ct,trap}} + R_{\text{trapping}}} \quad (6)$$

Where k_{ct} and k_{trapping} are the charge transfer and trapping rate constants, respectively. The charge transfer efficiency obtained from the PEIS data is shown in Figure 7D. The abnormally high transfer efficiency (TE) in the low applied potential region (before the onset potential) might be due to deviations of the charge transfer kinetic models at the region, where the effect of SS is less prevalent.^{10, 62} In essence, although the application of ITO underlayer provides an additional Sn doping amount, it does not affect the rate of surface electron-hole recombination at Fe₂O₃|electrolyte interface, evidenced by the same trend of TE values in the Fe₂O₃ and ITO/Fe₂O₃ electrodes. In both cases, significant surface electron-hole recombination is expected. The surface electron-hole recombination in the ITO/Fe₂O₃/Fe₂TiO₅ and ITO/Fe₂O₃/Fe₂TiO₅/FeNiOOH electrodes has been suppressed; and in the case of the ITO/Fe₂O₃/Fe₂TiO₅/FeNiOOH electrode, over 80 % of the holes are being transferred into the electrolyte at 1.23V vs RHE. The calculated TE values of these electrodes also agree well with the steady-state current-voltage relationship (Figure 5A). Our result here highlights the effectiveness of the atomic level Fe₂TiO₅ and FeNiOOH nanodots coating on regulating the surface state density and energy level of hematite nanowires as well as reducing the surface electron-hole recombination rate to speed up its water oxidation rate.

3. Conclusions

In summary, an ITO/Fe₂O₃/Fe₂TiO₅/FeNiOOH nanowires electrode with a quaternary multilayer heterostructure^{10, 20, 30, 47, 50, 51, 57} successfully integrated by a stepwise deposition of ITO underlayer, ultrathin Fe₂TiO₅ and FeNiOOH nanodots onto Fe₂O₃ nanowires. The resulting quaternary multilayer nanowires exhibit significantly enhanced PEC performance, including a large photocurrent (2.2 mA cm⁻²) and a high stability. A deep and careful investigation into the mechanism responsible for the enhanced PEC performance has been conducted. These studies show that: (i) the ITO underlayer is used as a high quality electrical back contact to reduce the back-contact interface charge recombination and as a Sn doping source for tuning the donor density, (ii) atomic level Fe₂TiO₅ coating, serves as the surface state density and energy level modulation layer, effectively suppresses the charge recombination at the semiconductor junction interface, (iii) the FeNiOOH nanodots, increase the surface active sites, and thus accelerates the OER kinetics at the SEI. The interfacial coupling effect between the ITO underlayer, the ultrathin Fe₂TiO₅ and the FeNiOOH nanodots in the ITO/Fe₂O₃/Fe₂TiO₅/FeNiOOH photoanodes simultaneously enhances the charge separation and water oxidation efficiency, and suggest a path forward to design improved integrated photoanodes.

4. Experimental

4.1 Chemicals and Materials.

All commercially available reagents and solvents were used as received without further purification unless otherwise indicated. All chemical reagents were purchased from Sigma-Aldrich. If not specified, all solutions were prepared with Milli-Q water (ca. 18.2 MΩ·cm resistivity). Fluorine-tin-oxide (FTO) coated glass substrate (735167-1EA, 7 Ω/sq) was purchased from Sigma-Aldrich.

4.2 Electrode preparation.

FTO substrates were cut into small pieces with 1 cm × 3 cm area and washed by sonicating in a (1: 1: 1) mixture of acetone (Sigma-Aldrich, 99.9%), isopropanol (Sigma-Aldrich, 99.9%) and water. After rinsing the FTO substrates thoroughly with distilled water, the substrates were washed in ethanol (Fluka, 99.8%) and then dried in air at 300 °C for 1 h (heating rate: 8.5 °C min⁻¹). A part of the substrates (ca. 1 cm × 2 cm) was covered using a polymer tape (Kapton® Foil, VWR International) prior to the following process. The uncoated part of the FTO was later employed as electric contact for the electrodes in the photo-electrochemical cell.

Fe₂O₃ electrodes. Hematite nanowires were prepared following a slightly adapted procedure.⁴⁷ A 200 ml Teflon-lined stainless steel autoclave was filled with 60 ml aqueous solution containing 0.15 M ferric chloride (FeCl₃, 97%) and 1 M sodium nitrate (NaNO₃, 99%) and 316 μL hydrochloric (HCl, wt 37%). Six pieces of washed FTO substrates were put into the autoclave and heated at 95 °C for 4 hours. A uniform layer of iron oxyhydroxides (FeOOH) nanowires was formed on the FTO substrate, as displayed in Figure S32. The FeOOH-coated substrate was then washed with deionized water to remove any residual salt, and subsequently sintered in air at 550°C (heating rate: 8.5°C min⁻¹) for 2 hours. During this pre-sintering process, the FeOOH nanowires were converted into hematite nanowires without deterioration of the nanowires structure, as shown Figure S33. To further reduce the surface defective sites, the

ARTICLE

Energy & Environmental Science

hematite nanowires were treated at 750 °C for additional 30 min and subsequently quenched in air within 1 min (post-quenched process).

ITO/Fe₂O₃ electrodes. Different thickness (49 nm, 105 nm, 149 nm, 196 nm and 245 nm) of indium doped tin dioxide (ITO, In₂O₃: SnO₂= 90/10 wt %) were deposited onto the FTO substrate by DC-pulsed sputtering according to our previous report.⁶³ After that, the ITO coated FTO substrates were subjected to the same hydrothermal and pre-sintering process for Fe₂O₃ electrode as described above to grow hematite nanowires on the surface of ITO/FTO substrates. For the post-quenched process of ITO/Fe₂O₃, a quenched condition at 750 °C for 30 min has been employed.

ITO/Fe₂O₃/Fe₂TiO₅ electrodes. The obtained ITO/Fe₂O₃ samples after pre-sintering process were further subjected to TiO₂ atomic layer deposition (ALD) process.⁶⁴ The ALD was performed in R200 Picosun Atomic Layer Deposition system at 150°C with TiCl₄ (Sigma-Aldrich, 99%) and water as the precursors in an 8 mbar N₂ flow atmosphere, reaching a growth rate of 0.27 Å cycle⁻¹. The typical pulse time for the TiCl₄ and water was 0.1 s and the purge time was 10 s. The TiO₂ thickness of ITO/Fe₂O₃/Fe₂TiO₅ electrode was controlled by changing the deposition cycle, i.e., 15 cycles, 30 cycles, 50 cycles, 100 cycles and 150 cycles. After that, a varying quenched time slot (10 min, 30 min, 40 min and 80 min) at 750 °C has been tuned to optimize the sintering condition and transform the ALD TiO₂ into Fe₂TiO₅.

ITO/Fe₂O₃/Fe₂TiO₅/FeNiOOH electrodes. The optimized ITO/Fe₂O₃/Fe₂TiO₅ electrodes were further coated with FeNiOOH via photo-electrodeposition.^{18, 39, 41, 54} Photo-electrodeposition of FeNiOOH on the ITO/Fe₂O₃/Fe₂TiO₅ electrodes were carried out in a mixture solution containing 0.01 M FeSO₄·7H₂O (≥99%) and 0.1 M NiSO₄·6H₂O (99%). Prior to the photo-electrodeposition of FeNiOOH, the solution was purged with nitrogen gas for 30 min. A three-electrode cell was used, composed of an ITO/Fe₂O₃/Fe₂TiO₅ electrode (work electrode), a Pt wire (counter electrode), and a Ag/AgCl (3 M KCl, reference electrode). A 150 W AM 1.5G solar simulator (Solar Light Co., 16S-300-002 v4.0) with an incident light intensity set at 1 Sun (100 mW cm⁻²) was used as the light source, and the light density was calibrated using a thermopile (Gentec-EO, XLPF12-3S-H2-DO) coupled with an optical power meter (Gentec-EO UNO). The light was illuminated through the glass side (back-side illumination) and the light intensity was 100 mW cm⁻². For clarification, the FeOOH grown on the back side of the FTO glass during the hydrothermal process has been carefully removed for all samples by lens wiping paper before the sintering treatment. To facilitate the photoelectrodeposition, an external bias of ca. 0.25 V vs Ag/AgCl (3M KCl) was applied. During illumination, the holes generated in the valence band of Fe₂O₃ were used to oxidize Fe²⁺/Ni²⁺ ions to Fe³⁺/Ni³⁺ ions, which precipitate as FeNiOOH on the surface of the ITO/Fe₂O₃/Fe₂TiO₅ electrode (Fe²⁺/Ni²⁺(aq) + h⁺ + 3OH⁻ → FeNiOOH(s) + H₂O).^{18, 54} Various deposition charges (i.e., 5 mC, 10 mC, 15 mC and 20 mC) were deposited onto the surface of the ITO/Fe₂O₃/Fe₂TiO₅ nanowires by controlling the deposition time. The fabrications process of the ITO/Fe₂O₃/Fe₂TiO₅/FeNiOOH electrode is displayed in Schematic 2.

4.3 Optical, structural and morphological characterization

The grazing incidence X-ray diffraction (XRD) analyses were performed on a Bruker D4 X-ray powder diffractometer using the Cu Ka radiation (1.54184 Å) and a 1D Lynkeye detector, which is equipped with a Gobel mirror in the incident beam and equatorial Soller slits in the diffracted beam (51 incidence angle, 2° step⁻¹). Optical properties of all electrodes were characterized by using a UV-vis spectrophotometer (Lambda 950, Perkin Elmer) equipped with an integrating sphere (150 mm diameter sphere covered with Spectralon as the reflecting material, Perkin Elmer). Absorbance (A) measurements were obtained from measured reflectance (R, %) and transmission (T, %), using a wavelength range of 350 to 800 nm and a step of 5 nm, respectively. The morphology of the films was characterized using a field emission gun scanning electron microscope (FE-SEM, Zeiss Series Auriga microscopy) equipped with an electron dispersive X-ray spectroscopy (EDX) detector. X-ray photoelectron spectroscopy (XPS) was performed with a Phoibos 150 analyser (SPECS GmbH, Berlin, Germany)) in ultra-high vacuum conditions (base pressure 4×10^{-10} mbar) with a monochromatic aluminium K_α X-ray source (1486.74 eV). The energy resolution as measured by the FWHM of the Ag 3d5/2 peak for a sputtered silver foil was 0.8 eV. All the samples for HRTEM and STEM were prepared by using a mechanical process, as displayed in Schematic S2 and published elsewhere.⁶⁵ HRTEM and STEM images have been obtained by using a FEI Tecnai F20 field emission gun microscope with a 0.19 nm point-to-point resolution at 200 kV equipped with an embedded Quantum Gatan Image Filter for EELS analyses. Images have been analysed by means of Gatan Digital Micrograph software. Atomic supercell modelling was performed by the Eje-Z, Rhodius and JMOL software packages with the corresponding crystal phase parameters of each species obtained from ICSD, which were verified by HRTEM and STEM-EELS mapping.⁶⁵⁻⁶⁸

4.4 Photo-electrochemical measurements

Photocurrent (j , mA cm⁻²) vs. potential (E, V) curves were taken using an undivided three-electrode cell. The working, counter and reference electrodes were the aforementioned composite hematite nanowires (1 cm² geometric area), a Pt wires and an Ag/AgCl (3M KCl) electrode (Metrohm, E=0.203 vs NHE), respectively. The electrolyte was a 1 M NaOH solution (pH 13.6). The electrolyte was purged with N₂ during the experiments. CV was taken using a computer-controlled potentiostat (VMP3, BioLogic Science Instruments). Potential was scanned from -0.45 V vs. Ag/AgCl to 0.85 V vs. Ag/AgCl, with a scan rate of 20 mV s⁻¹. The photocurrent density is referred to the geometric area. All potentials were corrected at 80% for the ohmic drop, which was determined using the automatic current interrupt (CI) method implemented by the potentiostat,¹⁵ and are converted and reported with respect to the reversible hydrogen electrode (RHE): E (V vs. RHE) = E (V vs. Ag/AgCl) + 0.0592x pH + 0.203. Light illumination was performed using a 150 W AM 1.5G solar simulator (Solar Light Co., 16S-300-002 v 4.0) with an incident light intensity set at 1 Sun (100 mW cm⁻²), as measured using a thermopile (Gentec-EO, XLPF12-3S-H2-DO) coupled with an optical power meter (Gentec-EO UNO). In the PEC characterization, the light came from the front side (electrode-electrolyte interface, front side illumination). PEIS data were acquired with an alternate current (AC) perturbation of 5 mV in amplitude and a 100 mHz to 1 MHz frequency range, both in the

dark and under illumination, and under selected direct current (DC) potentiostatic conditions (-0.45 to 0.85 V vs Ag/AgCl). Nyquist plots (imaginary vs. real components of impedance, Z_{Im} vs. Z_{Re}) were fitted to the corresponding equivalent circuits using Z-fit (BioLogic Associates). Fitted capacitances and resistances are referred to the electrode geometric area (1 cm × 1cm). Error bars stem from the goodness of the EIS data fittings.

4.5) Incident Photon to Current Efficiency (IPCE).

IPCE were characterized using a xenon light source (Abet 150 W Xenon Lamp) coupled with a monochromator (Oriel Cornerstone 260 1/4 m monochromator). The wavelength was scanned from 350 to 800 nm (step: 10 nm step⁻¹) keeping the voltage fixed at 1.23 V vs. RHE. To calculate IPCE, the following relation was used:⁵⁵

$$\text{IPCE (\%)} = (1240/\lambda) \times (I/J_{\text{light}}) \times 100 \quad (7)$$

Where I is the photocurrent density (mA cm^{-2}) obtained using a potentiostat (mentioned earlier) recording the i-t curve at 1.23 V vs. RHE, λ is the incident light wavelength (nm) from monochromatic, and J_{light} (mW cm^{-2}) is the power density of monochromatic light at a specific wavelength. A source meter (Keithley Instruments Inc., model no. 2400) coupled with the standard Silicon Photodiode (Thorlabs, S120VC) was used to measure the power density of monochromatic light.

Author contribution

PengYi Tang, Jordi Arbiol and Joan Ramon Morante designed the experiments. PengYi Tang carried out the XRD, UV-Vis Spectrum, SEM, EDS, TEM, STEM-EELS maps, the atomic supercell models, hydrothermal reaction, sintering process, photo-electrodeposition, and electrochemical experiments. HaiBing Xie, Alejandro Pérez Rodríguez and Edgardo Saucedo carried out the ITO sputtering experiments. Carles Ros, Martí Biset-Peiró and Teresa Andreu carried the ALD TiO₂ deposition experiments. LiJuan Han and José Ramón Galán-Mascarós participated part of PEIS experiments and PEIS data analysis. Guillaume Sauthier carried out the XPS spectrum experiments. PengYi Tang, Jordi Arbiol, YongMin He, Wesley Kramer and Joan Ramon Morante co-wrote the manuscript and all authors edited the manuscript.

Acknowledgements

This work was supported by the Spanish Ministerio de Economía y Competitividad (MINECO, grant CTQ2015-71287-R) through coordinated Projects TNT-FUELS, and e-TNT (MAT2014-59961-C2), the BIST Ignite Project inWOC and the Generalitat de Catalunya (2014-SGR-797 and 2014-SGR-1638). Part of the present work has been performed in the framework of Universitat Autònoma de Barcelona Materials Science Ph.D. program. We acknowledge Dr. Guillaume Sauthier from the ICN2 for the XPS measurements. ICN2 and ICIQ acknowledge support from the Severo Ochoa Program (MINECO, Grant SEV-2013-0295 and SEV-2013-0319). ICN2 and ICIQ are funded by the CERCA Programme / Generalitat de Catalunya.

References

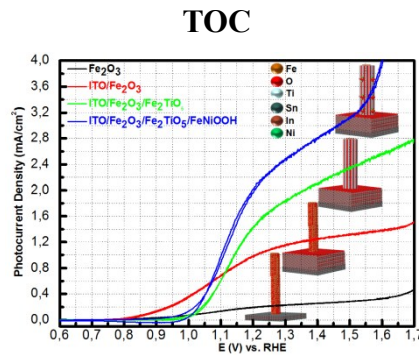
[1] K. Sivula, R. V. D. Krol. *Nature Rev. Mater.*, 2016, **1**, 15010.

- [2] S. H. Shen, S. A. Lindley, X. Y. Chen, J. Z. Zhang, *Energy Environ. Sci.*, 2016, **9**, 2744-2775. [View Article Online](#) DOI: 10.1039/C7EE01475A
- [3] Z. Q. Huang, Y.J. Lin, X. Xiang, W. Rodríguez-Córdoba, K. J. McDonald, K. S. Hagen, K. S. Choi, B. S. Brunschwig, D. G. Musaev, C. L. Hill, D.W. Wang, T.Q. Lian, *Energy Environ. Sci.*, 2012, **5**, 8923-8926.
- [4] S. R. Pendlebury, A. J. Cowan, M. Barroso, K. Sivula, J. H. Ye, M. Grätzel, D. R. Klug, J. W. Tang, J. R. Durrant, *Energy Environ. Sci.*, 2012, **5**, 6304-6312.
- [5] T. A. Pham, Y. Ping, G. Galli, *Nature Mater.*, 2017, **16**, 401-408.
- [6] J. T. Li, S. K. Cushing, P. Zheng, F.K. Meng, D. Chu, N.Q. Wu, *Nature Commun.*, 2013, **4**, 2651.
- [7] M. E. McBriarty, G. F. V. Rudorff, J. E. Stubbs, P. J. Eng, J. Blumberger, K. M. Rosso, *J. Am. Chem. Soc.*, 2017, **139**, 2581-2584.
- [8] B. Iandolo, B. Wickman, E. Svensson, D. Paulsson, A. Hellman, *Nano Lett.* 2016, **16**, 2381-2386.
- [9] Y. C. Qiu, S. F. Leung, Q. P. Zhang, B. Hua, Q. F. Lin, Z. H. Wei, K. H. Tsui, G. Zhang, S. H. Yang, Z. Y. Fan, *Nano Lett.* 2014, **14**, 2123-2129.
- [10] D. M. Satoca, M. Bartsch, C. Fabrega, A. Genç, S. Reinhard, T. Andreu, J. Arbiol, M. Niederberger, J.R. Morante, *Energy Environ. Sci.*, 2015, **8**, 3242-3254.
- [11] Y.J. Lin, S. Zhou, S. W. Sheehan, D.W. Wang, *J. Am. Chem. Soc.* 2011, **133**, 2398-2401.
- [12] I. S. Cho, H. S. Han, M. Logar, J. Park, X. L. Zheng, *Adv. Energy Mater.* 2015, 1501840.
- [13] A. Annamalai, A. Subramanian, U. Kang, H. Park, S. H. Choi, J. S. Jang, *J. Phys. Chem. C* 2015, **119**, 3810-3817.
- [14] P. S. Shinde, A. Annamalai, J. H. Kim, S. H. Choi, J. S. Lee, J. S. Jang, *Solar Energy Materials & Solar Cells*, 2015, **141**, 71-79.
- [15] L.J. Han, P.Y. Tang, A. Reyes-Carmona, B. Rodriguez-Garcia, M. Torrens, J. R. Morante, J. Arbiol, J. R. Galan-Mascaros, *J. Am. Chem. Soc.*, 2016, **138**, 16037-16045.
- [16] F. Song, X. Hu, *Nat. Commun.* 2014, **5**, 4477.
- [17] Y. Zhao, X. Jia, G. Chen, L. Shang, G. I. Waterhouse, L. Z. Wu, C. H. Tung, D. O'Hare, T. Zhang, *J. Am. Chem. Soc.* 2016, **138**, 6517-6524.
- [18] T. W. Kim, K. S. Choi, *Science*, 2014, **343**, 990-994.
- [19] L. Wang, F. Dionigi, N. T. Nguyen, R. Kirchgeorg, M. Gliech, S. Grigorescu, P. Strasser, P. Schmuki, *Chem. Mater.* 2015, **27**, 2360-2366.
- [20] K. G. U. Wijayantha, S. Saremi-Yarahmadi, L. M. Peter, *Phys. Chem. Chem. Phys.*, 2011, **13**, 5264-5270.
- [21] B. Klahr, S. Gimenez, F. Fabregat-Santiago, T. W. Hamann, J. Bisquert, *J. Am. Chem. Soc.*, 2012, **134**, 4294-4302.
- [22] Y. C. Zhang, H. N. Zhang, H. W. Ji, W. H. Ma, C. C. Chen, J. C. Zhao, *J. Am. Chem. Soc.*, 2016, **138**, 2705-2711.
- [23] Y. D. Su, C. L. Liu1, S. Brittman, J. Y. Tang, A. Fu, N. Kornienko, Q. Kong, P. D. Yang, *Nature Nano.*, 2016, **11**, 609-612.
- [24] J. B. Sambur, T.Y. Chen, E. Choudhary, G.Q. Chen, E. J. Nissen, E. M. Thomas, N. M. Zou, P. Chen, *Nature*, 2016, **530**, 77-80.
- [25] S. C. Warren1, K. Voïtchovsky, H. Dotan, C. M. Leroy, M. Cornuz, F. Stellacci, C. Hébert, A. Rothschild, M. Grätzel, *Nature Mater.*, 2013, **12**, 842-849.
- [26] O. Zandi, T. W. Hamann, *Nature Chem.*, 2016, **8**, 778-783.
- [27] Z. Zhang, J. T. YatesJr, *Chem. Rev.* 2012, **112**, 5520-5551.
- [28] B. Iandolo, A. Hellman, *Angew. Chem.* 2014, **53**, 13404-13408.
- [29] B. Klahr, T. Hamann, *J. Phys. Chem. C* 2014, **118**, 10393-10399.
- [30] T. Takashima, K. Ishikawa, H. Irie, *J. Phys. Chem. C* 2016, **120**, 24827-24834.
- [31] Q. H. Liu, J. F. He, T. Yao, Z. H. Sun, W. R. Cheng, S. He, Y. Xie, Y. H. Peng, H. Cheng, Y. F. Sun, Y. Jiang, F. C. Hu, Z. Xie, W. S. Yan, Z. Y. Pan, Z. Y. Wu, S. Q. Wei, *Nature Communications*, 2014, **5**, 5122.
- [32] M. R. Nellist, F. A. L. Laskowski, F. D. Lin, T. J. Mills, S. W. Boettcher, *Acc. Chem. Res.* 2016, **49**, 733-740.
- [33] Z. M. Zhang, C. T. Gao, Y. X. Li, W. H. Han, W. B. Fu, Y. M. He, E. Q. Xie, *Nano Energy*, 2016, **30**, 892-899.
- [34] J. Resasco, H. Zhang, N. Kornienko, N. Becknell, H. Lee, J. H. Guo, A. L. Briseno, P. D. Yang, *ACS Cent. Sci.* 2016, **2**, 80-88.

ARTICLE

Energy & Environmental Science

- [35] T. T. Yao, R. T. Chen, J. J. Li, J. F. Han, W. Qin, H. Wang, J. Y. Shi, F. T. Fan, C. Li, *J. Am. Chem. Soc.* 2016, **138**, 13664-13672.
- [36] I. Roger, M. A. Shipman, M. D. Symes, *Nature Rev. Chem.*, 2017, **1**, 3.
- [37] J. C. Hill, A. T. Landers, J. A. Switzer, *Nature Mater.*, 2015, **14**, 1150-1155.
- [38] F. D. Lin and S. W. Boettcher, *Nature Mater.*, 2014, **13**, 81-86.
- [39] M. W. Louie, A. T. Bell, *J. Am. Chem. Soc.* 2013, **135**, 12329-12337.
- [40] D. Friebel, M. W. Louie, M. Bajdich, K. E. Sanwald, Y. Cai, A. M. Wise, M.J. Cheng, D. Sokaras, T. C. Weng, R. Alonso-Mori, R. C. Davis, J. R. Bargar, J. K. Nørskov, A. Nilsson, A. T. Bell, *J. Am. Chem. Soc.* 2015, **137**, 1305-1313.
- [41] L. Trotochaud, S. L. Young, J. K. Ranney, S. W. Boettcher, *J. Am. Chem. Soc.* 2014, **136**, 6744-6753.
- [42] H. S. Ahn, A. J. Bard, *J. Am. Chem. Soc.* 2016, **138**, 313-318.
- [43] P.Y. Tang, L. J. Han, A. Genç, Y. M. He, X. Zhang, L. Zhang, J. R. Galán-Mascarós, J. R. Morante, J. Arbiol, *Nano Energy*, 2016, **22**, 189-201.
- [44] F. Y. Ning, M. F. Shao, S. M. Xu, Y. Fu, R. K. Zhang, M. Wei, D. G. Evans, X. Duan, *Energy Environ. Sci.*, 2016, **9**, 2633-2643.
- [45] Z. M. Zhang, C. T. Gao, Z. M. Wu, W. H. Han, Y. L. Wang, W. B. Fu, X. D. Li and E. Q. Xie, *Nano Energy*, 2016, **19**, 318-327.
- [46] A. Brauna, Y. L. Hu, F. Boudoirea, D. K. Bora, D. D. Sarmad, M. Grätzel, C. M. Eggleston, *Catalysis Today*, 2016, **260**, 72-81.
- [47] Y. C. Ling, G. M. Wang, D. A. Wheeler, J. Z. Zhang, Y. Li, *Nano Lett.*, 2011, **11**, 2119-2125.
- [48] J. Brillet, M. Gratzel, K. Sivula, *Nano Lett.* 2010, **10**, 4155-4160.
- [49] J. Y. C. Chen, L. N. Dang, H. F. Liang, W. L. Bi, J. B. Gerken, S. Jin, E. E. Alp, S. S. Stahl, *J. Am. Chem. Soc.* 2015, **137**, 15090-15093.
- [50] M. Görlin, P. Chernev, J. F. d. Araújo, T. Reier, S. Dresp, B. Paul, R. Krähnert, H. Dau, P. Strasser, *J. Am. Chem. Soc.* 2016, **138**, 5603-5614.
- [51] X. W. Yu, M. Zhang, W. J. Yuan, G. Q. Shi, *J. Mater. Chem. A*, 2015, **3**, 6921-6928.
- [52] J. J. Deng, X. X. Lv, H. Zhang, B. H. Zhao, X. H. Sun, J. Zhong, *Phys. Chem. Chem. Phys.*, 2016, **18**, 10453-10458.
- [53] J. J. Deng, X. X. Lv, K. Q. Nie, X. L. Lv, X. H. Sun, J. Zhong, *ACS Catal.*, 2017, **7**, 4062-4069.
- [54] K. J. McDonald, K. S. Choi, *Energy Environ. Sci.*, 2012, **5**, 8553-8557.
- [55] P. S. Bassi, R. P. Antony, P. P. Boix, Y.N. Fang, J. Barber, L. H. Wong, *Nano Energy*, 2016, **22**, 310-318.
- [56] B. Klahr, S. Gimenez, F. Fabregat-Santiago, J. Bisquert, T.W. Hamann, *J. Am. Chem. Soc.* 2012, **134**, 16693-16700.
- [57] B. Klahr, S. Gimenez, F. Fabregat-Santiago, J. Bisquert, T. W. Hamann, *Energy Environ. Sci.*, 2012, **5**, 7626-7636.
- [58] T. L. Villarreal, R. Gomez, M. Neumann-Spallart, N. Alonso-Vante and P. Salvador, *J. Phys. Chem. B*, 2004, **108**, 15172-15181.
- [59] O. Zandi, T. W. Hamann, *J. Phys. Chem. Lett.*, 2014, **5**, 1522-1526.
- [60] Z. X. Su, J. S. Baskin, W. Z. Zhou, J. M. Thomas, A. H. Zewail, *J. Am. Chem. Soc.* 2017, **139**, 4916-4922.
- [61] B. H. Han, K. A. Stoerzinger, V. Tileli, A. D. Gamalski, E. A. Stach, S. H. Yang, *Nature Mater.*, 2017, **16**, 121-126.
- [62] W. Li, D. He, S. W. Sheehan, Y. M. He, J. E. Thorne, X. H. Yao, G. W. Brudvig, D. W. Wang, *Energy Environ. Sci.*, 2016, **9**, 1794-1802.
- [63] M. Neuschitzer, Y. Sanchez, T. Olar, T. Thersleff, S. Lopez-Marino, F. Oliva, M. Espindola-Rodriguez, H. B. Xie, M. Placidi, V. Izquierdo-Roca, I. Lauerman, K. Leifer, A. Perez-Rodriguez, E. Saucedo, *Chem. Mater.*, 2015, **27**, 5279-5287.
- [64] C. Ros, T. Andreu, M. D. Hernández-Alonso, G. Penelas-Pérez, J. Arbiol, J. R. Morante, *ACS Appl. Mater. Interfaces*, 2017, DOI: 10.1021/acsami.7b02996.
- [65] M. D. L. Mata, R. Leturcq, S. R. Plissard, C. Rolland, C. Magen, J. Arbiol, P. Caroff, *Nano Lett.*, 2016, **16**, 825-833.
- [66] S. Bernal, F. J. Botana, J. J. Calvino, C. Lopez-Cartes, J. A. Perez-Omil and J. M. Rodriguez-Izquierdo, *Ultramicroscopy*, 1998, **72**, 135-164.
- [67] R. R. Zamani, M. Ibanez, M. Luysberg, N. Garcia-Castello, DOI: 10.1039/C4EE01475A
- [68] J. Arbiol, A. Cirera, F. Peiró, A. Cornet, J. R. Morante, J. J. Delgado and J. J. Calvino, *Applied Physics Letters*, 2002, **80**, 329-331.



Tuning the Donor density and the Surface State Density of Hematite Multilayer Nanowires Photoanode via Bottom-up Interfacial Engineering for Enhanced Photoelectrochemical Water Splitting